nature nanotechnology

ARTICLES

https://doi.org/10.1038/s41565-019-0363-8

Graphene acoustic plasmon resonator for ultrasensitive infrared spectroscopy

In-Ho Lee[1], Daehan Yoo[1], Phaedon Avouris[2], Tony Low[1] and Sang-Hyun Oh[1]*

One of the fundamental hurdles in plasmonics is the trade-off between electromagnetic field confinement and the coupling efficiency with free-space light, a consequence of the large momentum mismatch between the excitation source and plasmonic modes. Acoustic plasmons in graphene, in particular, have an extreme level of field confinement, as well as an extreme momentum mismatch. Here, we show that this fundamental compromise can be overcome and demonstrate a graphene acoustic plasmon resonator with nearly perfect absorption (94%) of incident mid-infrared light. This high efficiency is achieved by utilizing a two-stage coupling scheme: free-space light coupled to conventional graphene plasmons, which then couple to ultraconfined acoustic plasmons. To realize this scheme, we transfer unpatterned large-area graphene onto template-stripped ultraflat metal ribbons. A monolithically integrated optical spacer and a reflector further boost the enhancement. We show that graphene acoustic plasmons allow ultrasensitive measurements of absorption bands and surface phonon modes in ångström-thick protein and SiO_2 layers, respectively. Our acoustic plasmon resonator platform is scalable and can harness the ultimate level of light–matter interactions for potential applications including spectroscopy, sensing, metasurfaces and optoelectronics.

Plasmons in graphene[1–5] have been exploited for a wide range of applications, including optical modulators[6–8], photodetectors[9–13], metasurfaces[14–17], polarization control devices[18,19] and sensors[20–22]. Due to the weak light–matter interactions in atomically thin graphene[3,23], the operation of these devices primarily relies on the deep-subwavelength confinement of electromagnetic waves enabled by graphene plasmons (GPs) [24–26]. When graphene is placed in proximity to a metal surface, the charge oscillations within graphene are balanced by out-of-phase oscillations from image charges, generating acoustic graphene plasmons (acoustic GPs) characterized by a linear dispersion at small wavevectors. Acoustic GPs can generate an ultraconfined out-of-plane electric field in the gap between the graphene and the metal[27–29]. Recent observations of propagating acoustic GPs using near-field scanning optical microscopy showed extreme field confinement (around ×1,000) of free-space light at terahertz frequencies[30,31].

The tight confinement afforded by acoustic GPs is promising for surface-enhanced infrared absorption spectroscopy (SEIRA)[20–22,32], but also implies a very large momentum mismatch with free-space light and hence poor coupling efficiency. For SEIRA applications, a highly efficient far-field coupling scheme is essential to discriminate the weak vibrational fingerprints of thin-film analytes from background noise. Recently, acoustic GPs were used to demonstrate the ultimate limits of field confinement, but the extinction signal in the mid-infrared was relatively weak[33], which presents a challenge for SEIRA applications.

In this Article, we demonstrate a strategy to achieve acoustic GP resonators with dramatically improved plasmon resonances (measured absorption of 94%) by utilizing conventional GPs as an intermediary and by monolithically integrating an optical spacer and a back reflector. The large absorption enabled by our acoustic GP resonator, in turn, allows ultrasensitive detection of mid-infrared absorption bands from submonolayer protein films and plasmon–phonon coupling from ångström-thick SiO_2 layers using far-field Fourier-transform infrared measurements.

High-efficiency acoustic plasmon coupling mechanism

The acoustic GP resonator consists of a continuous graphene layer and a metal ribbon array separated by a nanogap (g) (Fig. 1a). The width of each metal ribbon and the spacing between adjacent ribbons are denoted by w and s, respectively, and the periodicity is given by $p=w+s$. The unit cell of the acoustic GP resonator consists of two sections, with and without the metal underneath the graphene layer. The metal-coupled region supports acoustic GPs and the metal-free region supports GPs. Due to the presence of a continuous graphene layer, acoustic GPs can be launched not only through scattering-mediated coupling (κ_{01}) but also through the plasmon conversion process from GPs with smaller momenta (κ_{21}), which can be more efficiently excited from the scattered fields (κ_{02}). Here, κ_{ij} denotes the coupling coefficient from the i to j mode, where $i,j\in\{0, 1, 2\}$ represent the free-space wave, acoustic GP and GP modes, respectively. For a normally incident plane wave with transverse magnetic (TM) polarization, the electric field enhancement of the plasmons in our device can be approximated as follows (Supplementary Fig. 1):

$$\frac{E_{\mathrm{p}}}{E_{\mathrm{inc}}} \approx \begin{cases} (\kappa_{01} + \kappa_{02}\kappa_{21}e_2)(1 - \kappa_{12}\kappa_{21}e_1e_2)^{-1}, & 0<x<w \\ (\kappa_{02} + \kappa_{01}\kappa_{12}e_1)(1 - \kappa_{12}\kappa_{21}e_1e_2)^{-1}, & -s<x<0 \end{cases} \quad (1)$$

where $e_1=\exp(ik_1w)$ and $e_2=\exp(ik_2s)$. E_{inc} and E_{p} are the x components of the electric field magnitudes for the incident waves and the plasmons propagating in the x direction, respectively. From equation (1), the resonance condition is given as

$$k_1w+k_2s+\Phi_{12}+\Phi_{21}=2l\pi \quad (2)$$

where k_1 and k_2 denote the momentum of the acoustic GPs and GPs, respectively, and l is an integer that represents the order of the resonance. Φ_{12} and Φ_{21} are the phases of κ_{12} and κ_{21}, respectively, which are close to 0 (Supplementary Figs. 2 and 3). Similarly, the

[1]Department of Electrical and Computer Engineering, University of Minnesota, Minneapolis, MN, USA. [2]IBM T. J. Watson Research Center, Yorktown Heights, New York, NY, USA. *e-mail: sang@umn.edu

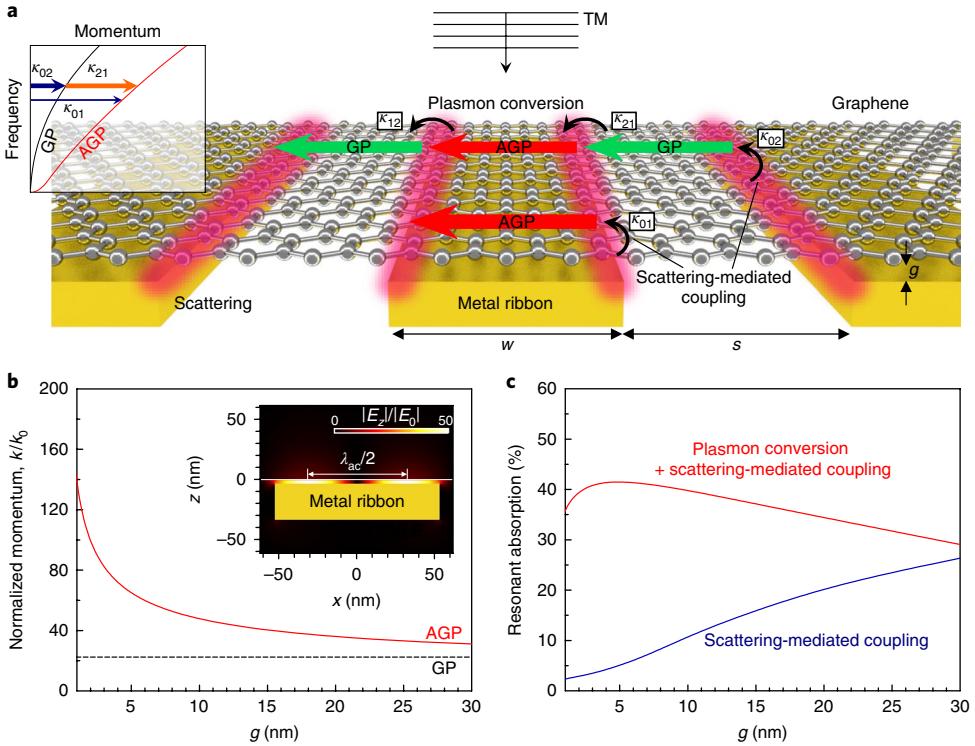

Fig. 1 | Coupling mechanisms. a, Schematic illustration of the acoustic plasmon resonator architecture and coupling routes to plasmon modes for a plane wave normally incident with TM polarization. Red and green arrows represent acoustic GPs (AGPs) and conventional GPs (GPs), respectively. κ_{ij} denotes the coupling coefficient from the i to j mode where $i,j \in \{0, 1, 2\}$ represent free-space waves, AGPs and GPs, respectively, and g is the gap distance between the graphene layer and metal ribbons. Inset, Typical plasmon dispersions for AGPs and GPs in the free-standing case. **b**, The gap dependence of AGP plasmon momentum k normalized to the free-space momentum k_0 at the free-space wavelength of 8 μm. Inset, Typical near-field distribution for the AGP resonator for $g = 3$ nm (freestanding case). **c**, Resonant absorption as a function of gap size for the scattering-mediated coupling scheme and the plasmon conversion scheme at the free-space wavelength of 8 μm. In **b** and **c**, we assume that the gap is filled with alumina.

reflection amplitude across the metal-coupled and metal-free interfaces can also be neglected in this simple model because the maximum reflectance only approaches 30% for the parameters relevant in our experiments. The small reflectance in our scheme contrasts with the case of GPs reflected by the physical edge of graphene, where the reflectance approaches almost 100% with a non-trivial reflection phase of approximately -0.75π (ref. [34]). The numerators in equation (1) imply that the contributions from plasmon conversions ($\kappa_{02}\kappa_{21}e_2$ and $\kappa_{01}\kappa_{12}e_1$) boost the plasmon enhancement on top of the scattering-mediated coupling. Due to the extreme vertical confinement of both acoustic and conventional GPs, the plasmon conversion process (κ_{12} and κ_{21}) is highly efficient (Supplementary Fig. 2). In addition, κ_{02} is larger than κ_{01} due to the smaller momentum mismatch between GPs and scattered fields as well as the better mode overlap between them (Supplementary Figs. 4–6). Thus, the overall coupling coefficient for acoustic GPs is largely determined by $\kappa_{02}\kappa_{21}e_2$ for small k_2s. The mechanism based on the plasmon conversion process is a key feature of the present design. Analytical calculations (Fig. 1b) show that the momentum of an acoustic GP mode (red line) increases with decreasing g at a given frequency compared with the momentum of a GP mode (black dashed line). As illustrated in Fig. 1c, the present design retains high resonant absorption irrespective of g, thereby eliminating the trade-off with the momentum mismatch between acoustic GPs and free-space waves (red line). In contrast, the resonator design with graphene ribbons on metal ribbons (Supplementary Fig. 7), which relies only on the scattering-mediated coupling process (blue line), rapidly loses efficiency as the gap size shrinks.

In addition to the plasmon conversion process, the resonant absorption of the acoustic GP resonator can be further boosted by placing a reflector at a certain distance below the metal ribbons to recouple the transmitted waves back to the plasmon modes (Fig. 2a). Similar approaches have been employed to enhance the resonant absorption in graphene ribbon resonators[35,36]. The absorption enhancement by recoupling can be substantial due to large transmittance through the array of metal ribbons for TM polarization (Supplementary Fig. 8). The resonant absorption is maximized when the acoustic plasmon resonance is aligned to the critical wavelength λ_c that satisfies the 'quarter-wavelength condition'. At this condition, the total phase retardation of an electromagnetic wave after a round trip inside an optical spacer becomes π, hence maximizing the electric field at the resonator. The required thickness of an optical spacer (refractive index n_s) for the quarter-wavelength condition is $d = \lambda_c/(4n_s)$ or, equivalently, $d = 1/(4n_s\nu_c)$ using the critical wavenumber ν_c.

The effect of adding a reflector and optical spacer is analysed in Fig. 2b,c. Without a reflector (Fig. 2b), the resonant absorption intensities calculated for free-standing devices with different w are around 40%. With a reflector (Fig. 2c), on the other hand, the resonant absorption increases by a factor of more than two and becomes nearly 100% when the plasmon resonance approaches $\nu_c = 1{,}150\,\mathrm{cm}^{-1}$ (red line). The resonance wavelengths do not shift in the presence of a reflector, indicating that the coupling mechanism in the resonator part does not interfere with the absorption enhancement by the quarter-wavelength condition. Note that, even without graphene, the enhanced absorption in the substrate and

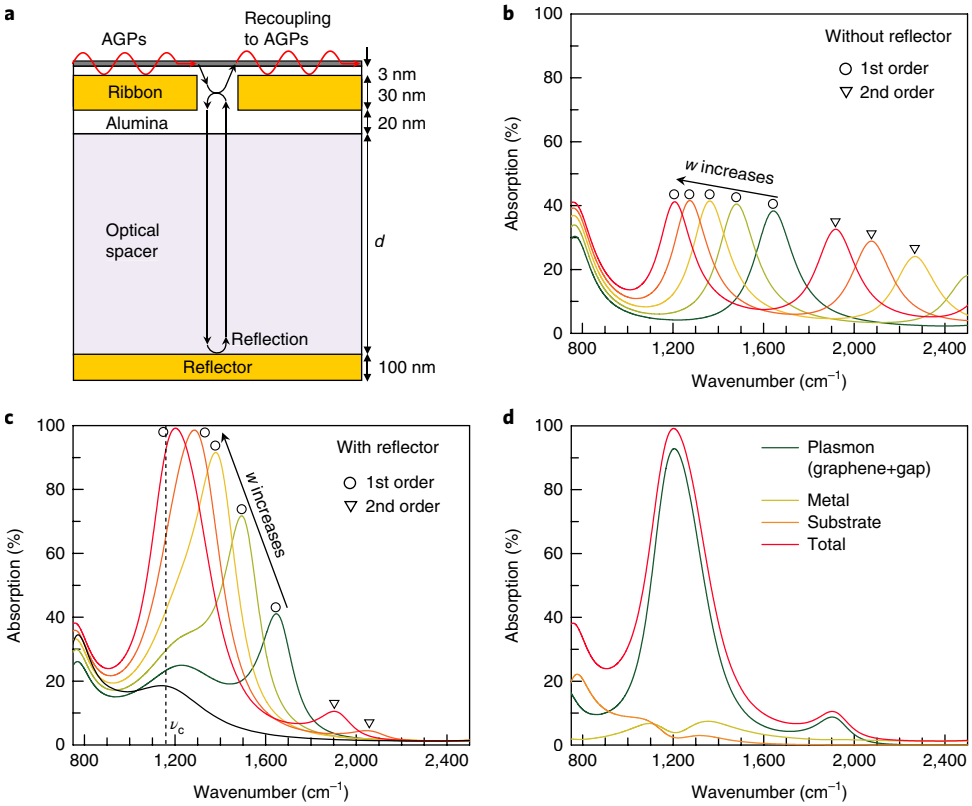

Fig. 2 | Plasmonic absorption enhancement by an integrated reflector. a, Schematic illustration of the mechanism for plasmonic absorption enhancement using the quarter-wavelength condition, that is, $\nu_c = (4n_s d)^{-1}$, where ν_c and n_s are the critical wavenumber that satisfies the quarter-wavelength condition and the refractive index of the optical spacer, respectively. **b**,**c**, Numerical results for absorption spectra from acoustic GP resonators without (**b**) and with (**c**) an optical spacer and reflector. **d**, Absorption contributions from the different parts of the resonator with $w = 85$ nm. In all cases, we used alumina as a gap-filling material with a gap size of 3 nm. s is fixed to be 20 nm and w varies from 45 nm to 85 nm in intervals of 10 nm (from green to red). In **c** and **d**, $n_s = 3.3$ and $d = 580$ nm. The absorption contributions are calculated from the power dissipation by integrating $\frac{1}{2P_0}\omega\varepsilon_0\Im(\varepsilon_r)|\mathbf{E}|^2$ over the region of interest, where ω, ε_0, $\Im(\varepsilon_r)$ and P_0 are angular frequency, vacuum permittivity, the imaginary part of relative permittivity and incident power per unit length, respectively. Because acoustic GPs store most of their electromagnetic fields in the graphene and gap regions, the plasmonic contribution to the resonant absorption is the sum of the power dissipation in both parts (green solid line).

metal parts manifests as a peak in the absorption spectrum around ν_c (black curve). Thus, it is important to investigate how the power dissipation through the substrate and metal parts competes with the dissipation via plasmons in the presence of graphene. As shown in Fig. 2d, the absorption in the substrate (orange line) and metal parts (yellow line) is greatly suppressed in the presence of graphene and the plasmonic absorption becomes a dominant contributor (94% of the total resonant absorption). This result shows that, even after integration with an optical spacer and reflector, the optical response of the entire system is dominated by the monolayer graphene and nanogap region near the top surface.

Fabrication of the acoustic graphene plasmon resonator

The main fabrication challenge in implementing our acoustic plasmon resonator is producing an ultraflat substrate in the presence of the uneven topography resulting from the underlying metal ribbons. Our numerical results show that such unevenness or surface roughness can significantly attenuate far-field signals (Supplementary Fig. 9). For sensing applications, it is also essential to have a graphene layer exposed at the top of the device to enable interaction between the plasmons and the target materials. We overcome these challenges by using a technique known as template stripping[37,38], which allows the high-throughput fabrication of ultrasmooth patterned metals by replicating them via a reusable silicon template. The detailed fabrication process based on template stripping is illustrated in Fig. 3a–c (also see Methods). As shown in the final device structure in Fig. 3d, this fabrication process also allows the monolithic integration of an optical spacer and a reflector, which makes it possible to enhance plasmonic signals via the quarter-wavelength condition[35,36].

The cross-sectional scanning electron microscopy (SEM) image in Fig. 3e shows that functional layers are well defined after the fabrication process. The optical micrograph of the final device in Fig. 3f shows that the top surface and underlying patterns are free from damage after template stripping (see Supplementary Fig. 10 for the Raman spectrum of graphene). The SEM image taken for $p = 200$ nm shows typical metal ribbons. The length of each ribbon along its long axis is 100 μm, which is about ten times larger than the operating wavelengths and allows us to describe the plasmonic responses of the resonator in the two-dimensional (2D) framework. Also, we designed s to be as small as possible in order for the contribution of acoustic GPs to be dominant over that of GPs and maximize resonant absorption by increasing the plasmon conversion contribution (Supplementary Fig. 11). Despite the presence of the ribbon patterns, the root-mean-square (r.m.s.) roughness of the template-stripped resonator surface measured by atomic force microscopy (AFM) is 0.75 nm (Supplementary Fig. 12).

Gap dependence of dispersion and absorption

Figure 4a shows the absorption spectra for different values of g ranging from 3 nm to 20 nm for $w = 180$ nm. As shown in the figure,

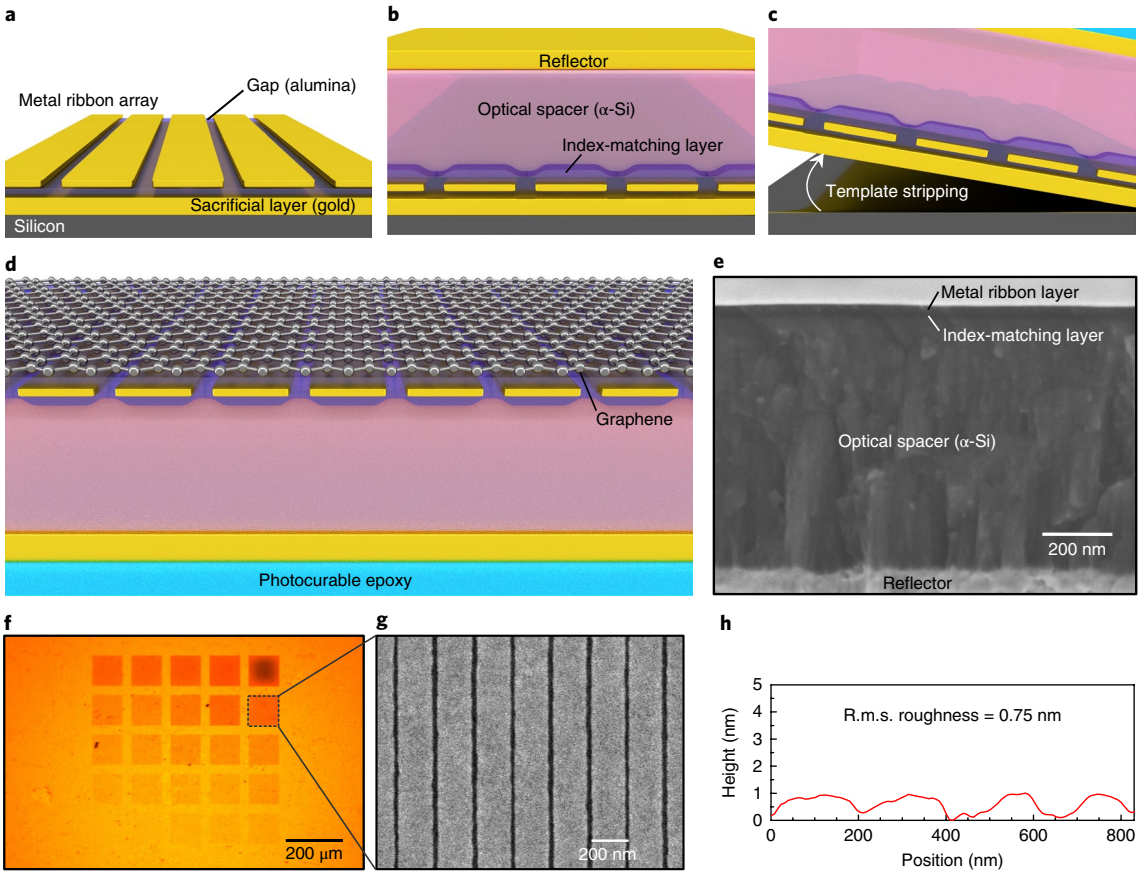

Fig. 3 | Fabrication process and resonator structure. a, Patterning an array of gold ribbons via electron-beam lithography on top of an alumina layer and sacrificial gold layer deposited on a silicon substrate. **b**, Sequential deposition of alumina, amorphous silicon and gold films as an index-matching layer, optical spacer and back reflector, respectively. **c**, Template stripping to expose the ultraflat interface between the bottom alumina and sacrificial layer using photo-curable epoxy as a backing layer. **d**, Schematic of the final device structure. **e**, Cross-sectional SEM image of the final device. **f**, Optical micrograph of the top surface of the resonator with an array of metal ribbons with different periodicities. **g**, SEM image of ribbons (180 nm width, 20 nm spacing and 20 nm gap size). **h**, Surface morphology of the ribbons taken by AFM.

the resonance shifts to longer wavelengths with decreasing g as the plasmon momentum increases at a given frequency. As the plasmon resonance approaches ν_c, the resonant absorption increases, consistent with the numerical results in Fig. 2c. From the absorption spectra for different w, we extract the plasmon dispersions using the relation $k_1 \approx 2\pi/(w+s)$, which is valid for $k_2 s \ll 1$. The plasmon momenta estimated from the absorption spectra increase with decreasing g and agree well with the analytical dispersions (Fig. 4b and Supplementary Fig. 13). The inset in Fig. 4b shows that the plasmon momentum scales as $g^{-1/2}$ at a given frequency, as predicted by theory[30,31,39]. In our experimental regime, we observe a normalized momentum k_1/k_0 of up to 91 for the $g = 3$ nm case at a frequency of 1,450 cm^{-1}, which is three times larger than that of GPs. The dispersion converges asymptotically to the phonon energy at small momentum, due to coupling with the surface phonons of alumina that occurs around 900 cm^{-1}. Our theoretical analysis implies stronger interactions with the phonons as the plasmon confinement becomes tighter[4] (Supplementary Fig. 14).

In Fig. 4c we compare the absorption spectra from acoustic GP resonators with different g but almost identical resonance frequencies near 1,170 cm^{-1}. In all cases we observe nearly perfect absorption (up to 94% for the 8 nm case, solid orange line) of incoming waves polarized perpendicular to the long axis of the metal ribbons. In addition to such a strong resonant absorption, we anticipate that the light–matter interaction by acoustic GPs can be further enhanced by reducing the damping of plasmons using higher quality graphene, encapsulating graphene with hexagonal boron nitride or using multilayer graphene. In contrast to a scattering-mediated coupling scheme, the measured resonant absorption for the acoustic GP resonator is nearly constant in g because the coupling efficiency is largely determined by the plasmon conversion process. The quality factors for the plasmon resonances for different values of g range from 4.4 ($g = 8$ nm) to 5.3 ($g = 3$ nm), showing a weak dependence on plasmon confinement (Supplementary Fig. 15).

Ångström-thick film sensing

The sensing results for silk protein are shown in Fig. 5a–c. Here, we have used an unpolarized light source for better signal-to-noise ratios. To access the highly confined electric fields of acoustic GPs, we deposited the target films on a 5-nm-thick alumina film on top of metal ribbons before transferring a graphene sheet. A 5-nm-thick alumina film helps to retain a large plasmon signal by reducing the scattering of acoustic GPs from the surface roughness of a target film and also allows a fair comparison of spectra between the cases with and without a target film (Supplementary Fig. 16). We used the substrate for the acoustic GP resonator before transferring graphene as a control sample, which has a peak in its absorption spectrum at $\nu_c = 1{,}600$ cm^{-1}.

The absorption spectrum from the control sample spin-coated with a 2.4-nm-thick silk film in Fig. 5a (see Supplementary

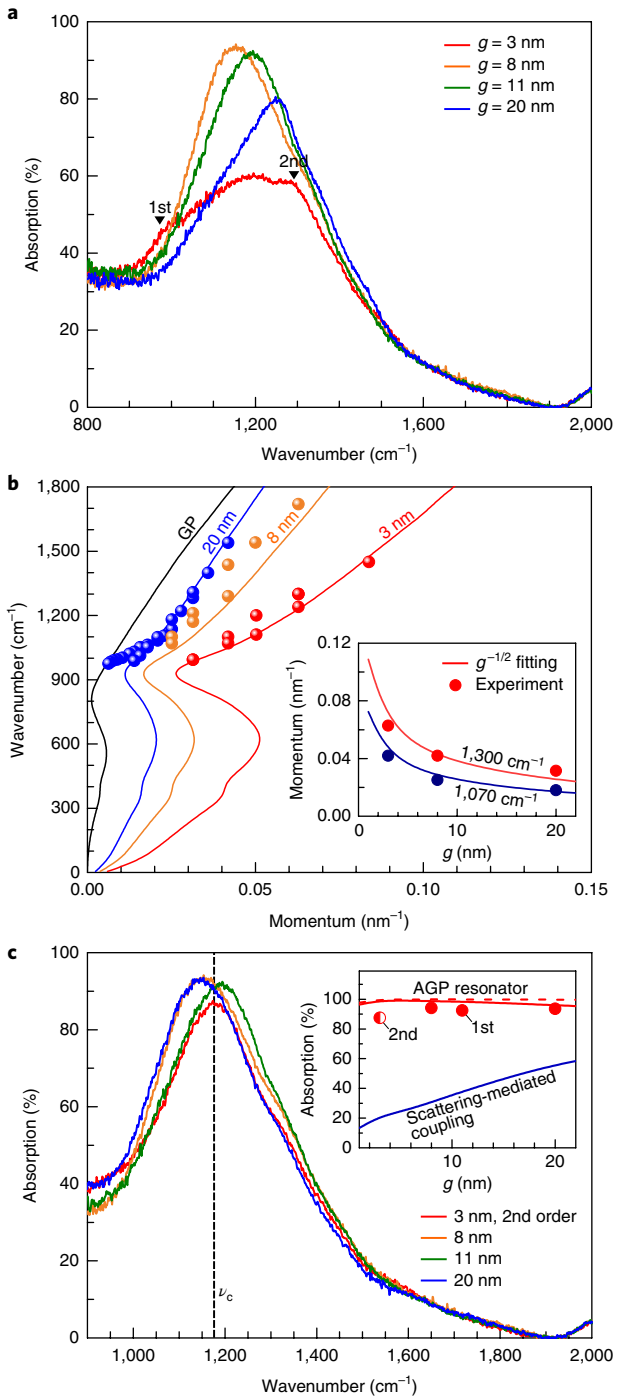

Fig. 4 | Gap dependence of dispersion and absorption. a, Plasmon absorption spectra for $g = 3$, 8, 11 and 20 nm with $w = 180$ nm and $s = 20$ nm. **b**, Gap-size-dependent plasmon dispersion. Inset, Dependence of momentum on g at resonant frequencies of 1,070 and 1,300 cm^{-1}. Solid lines represent the square root fitting of the experimental results (circles). **c**, Absorption spectra for different g where resonance frequencies are almost aligned around the critical wavenumber (ν_c) of 1,170 cm^{-1}. $w = 230$, 180, 180 and 230 nm with $s = 20$ nm for $g = 3$, 8, 11 and 20 nm, respectively. Inset, Resonant absorption as a function of g along with the numerical results for the plasmon conversion scheme (red solid and dashed lines represent the first and second order of resonance) and the scattering-mediated scheme (blue solid line).

Fig. 17 for silk thickness) shows only weak absorption signals (<1%) around the amide I and II bands at 1,650 and 1,546 cm^{-1}, respectively[40]. In acoustic GP resonators, the vibrational signals for the identical bands are an order of magnitude larger (13.2% and 11.6%) and clearly resolved with high signal-to-noise ratios (Fig. 5b, blue solid line) (see Supplementary Fig. 18 for extended results). Compared with the control device (without a target film inside the gap; pale blue solid line), the plasmon resonance shifts to a shorter wavelength in the presence of a silk film. This is largely due to the increase in the gap size and resultant decrease in plasmon confinement. The increase in the effective index of the gap is minimal because of the small index difference between silk and alumina ($|n_{silk} - n_{alumina}| < 0.2$) at the frequencies of interest. The inverted stack order and our 'graphene-last' transfer scheme minimize unwanted damage to analyte molecules. Although we insert target molecules/films in the nanogap between graphene and metal during the fabrication process in these proof-of-concept experiments, future developments of biosensing with acoustic GP-based SEIRA will require more practical sample insertion schemes.

Absorption for the amide I band is substantially larger than that reported for other configurations (for example, 3.5% for nanorod antennas with a 2 nm silk monolayer[41] and 0.7% for graphene ribbons with an 8 nm protein film[21]). Such strong light–matter interactions allow for the detection of submonolayer silk films. Because most of the coupled light is confined within the gap as an acoustic GP, the mode overlap with a 0.8-nm-thick film ($\sim\lambda_{freespace}/7{,}500$) is still on the order of 10%, which translates into a significant absorption signal as high as 3.6% for the amide I band (red solid line in Fig. 5b). The experimentally observed absorption signals for silk films are similar to the estimated values from the numerically fitted spectra shown in Fig. 5c. We expect that the sensitivity can be further enhanced by decreasing the thickness of the alumina film inside the gap.

The phonon–plasmon coupling results for an ångström-scale SiO_2 layer are shown in Fig. 5d–f. While the control sample shows no distinct features (Fig. 5d), a splitting of the plasmon resonance is observed in the absorption spectra taken from acoustic GP resonators with a 2 Å and 3 Å SiO_2 film (Fig. 5e). The 3 Å case shows a larger splitting of 102 cm^{-1} compared to 92 cm^{-1} for the 2 Å case, and a more distinct anti-crossing behaviour. We attribute the mode splitting behaviour to the coupling with longitudinal optical phonons[42–44]. The substantial resonance shift of 12 cm^{-1} (78 nm in wavelength) between the 2 Å and 3 Å cases illustrates the ångström-scale resolving power of our acoustic GP-based sensing platform (Fig. 5f).

Conclusions

By harnessing an efficient plasmon conversion process in a continuous graphene layer coupled with metal ribbons, graphene acoustic plasmon resonators can overcome the fundamental trade-off between field confinement and coupling efficiency. Our design is realized as a scalable device platform via template stripping, which enables the monolithic integration of ultraflat metal ribbons with an optical spacer and a backside reflector. A pristine graphene layer is transferred last in our scheme, thereby eliminating intrusive graphene ribbon patterning steps and minimizing other process-induced damages. This feature is also highly desirable for integrating other 2D materials that cannot withstand harsh processing conditions. Experimentally, we observed 94% absorption of incident mid-infrared light. By inserting analyte films into the plasmonic hotspots of acoustic GP resonators, we maximized their light–matter interactions and performed ultrasensitive detection of ångström-thick protein and dielectric films. The ability to generate ultraconfined and ultrastrong fields in a large-area chip, in addition to allowing high-signal-to-noise-ratio far-field detection, can benefit fundamental studies of general polariton physics in other 2D materials and their heterostructures[45] as well as nonlinear

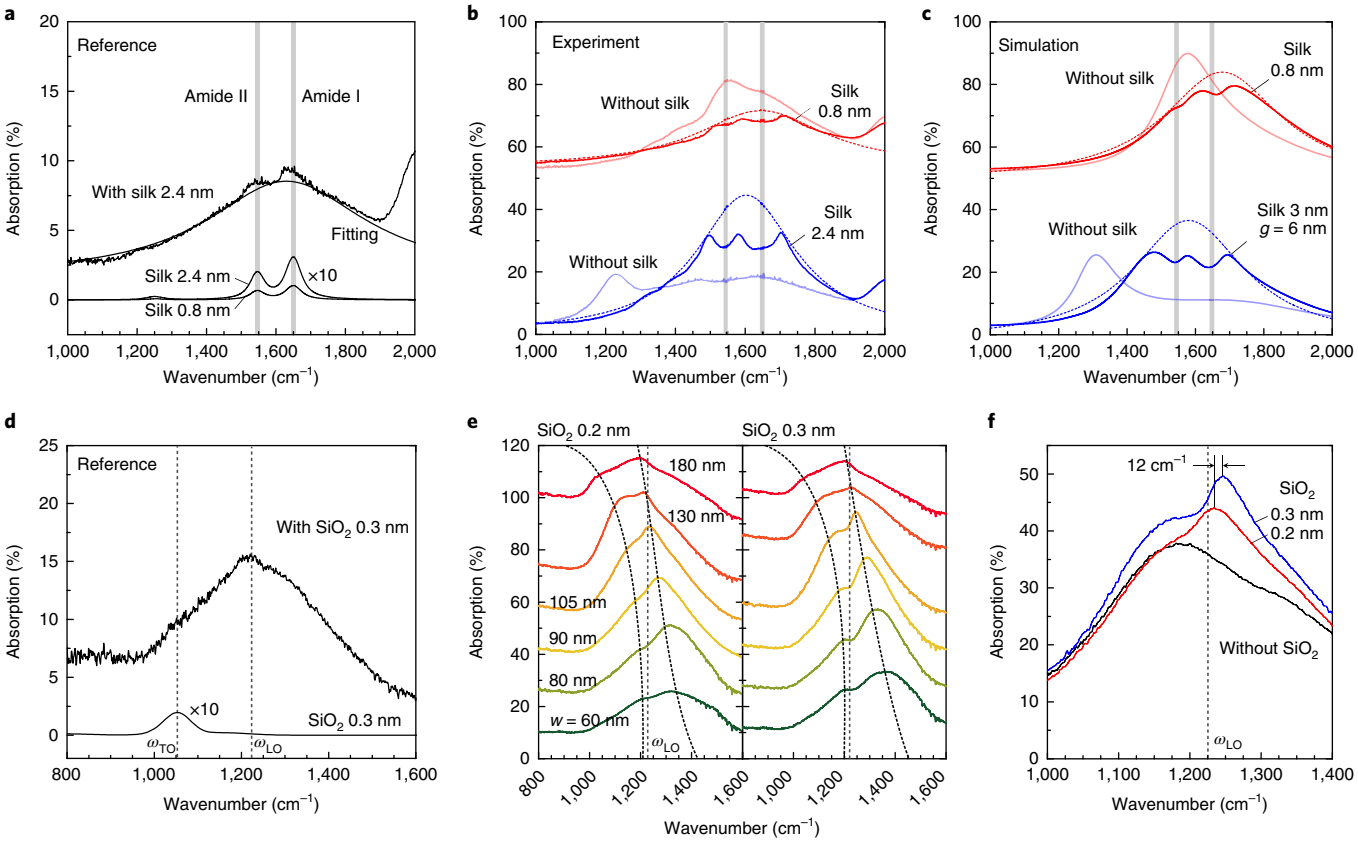

Fig. 5 | Acoustic-plasmon-mediated light–matter interactions. a, Reference absorption spectra for free-standing silk films (0.8 nm and 2.4 nm; numerical results, scaled ×10 for visibility), and a 2.4-nm-thick silk film on a template-stripped substrate without graphene. **b**, Measured absorption spectra from acoustic GP resonators coated with 0.8 nm and 2.4 nm silk films as well as the case without a silk film, and Lorentzian fitting curves (dashed lines). Here, $w = 60$ nm and $s = 30$ nm for the 0.8 nm case and $w = 90$ nm and $s = 30$ nm for the 2.4 nm case. **c**, Numerically calculated absorption spectra for comparison with the experimental results in **b** (for simulation details, see Supplementary Fig. 18). In **b** and **c**, the 0.8 nm case is shifted upwards. **d**, Reference absorption spectra for a free-standing 0.3 nm SiO_2 film (numerical results, lower curve) and the same film on a template-stripped substrate without graphene (measured data, upper curve). The longitudinal and transverse optical phonon frequencies of SiO_2, ω_{LO} and ω_{TO}, are denoted by grey dashed lines. **e**, Measured absorption spectra from acoustic GP resonators with 0.2 nm and 0.3 nm SiO_2 films for different w. **f**, Measured absorption spectra for different SiO_2 thickness for $w = 105$ nm. In **a** and **b**, $d = 450$ nm; in **d**–**f**, $d = 630$ nm.

effects[46–49]. This ability could also have strong impact on applications involving photodetectors[50], metasurfaces[17], light-emitting devices[51] and optical modulators[8,52].

Online content

Any methods, additional references, Nature Research reporting summaries, source data, statements of data availability and associated accession codes are available at https://doi.org/10.1038/s41565-019-0363-8.

Received: 2 August 2018; Accepted: 3 January 2019;
Published online: 11 February 2019

References

1. Hwang, E. & Sarma, S. D. Dielectric function, screening, and plasmons in two-dimensional graphene. *Phys. Rev. B* **75**, 205418 (2007).
2. Jablan, M., Buljan, H. & Soljačić, M. Plasmonics in graphene at infrared frequencies. *Phys. Rev. B* **80**, 245435 (2009).
3. Koppens, F. H., Chang, D. E. & García de Abajo, F. J. Graphene plasmonics: a platform for strong light–matter interactions. *Nano Lett.* **11**, 3370–3377 (2011).
4. Yan, H. et al. Damping pathways of mid-infrared plasmons in graphene nanostructures. *Nat. Photon.* **7**, 394–399 (2013).
5. Wunsch, B., Stauber, T., Sols, F. & Guinea, F. Dynamical polarization of graphene at finite doping. *New J. Phys.* **8**, 318 (2006).
6. Liu, M. et al. Graphene-based broadband optical modulator. *Nature* **474**, 64–67 (2011).
7. Sensale-Rodriguez, B. et al. Broadband graphene terahertz modulators enabled by intraband transitions. *Nat. Commun.* **3**, 780 (2012).
8. Sun, Z., Martinez, A. & Wang, F. Optical modulators with 2D layered materials. *Nat. Photon.* **10**, 227–238 (2016).
9. Fang, Z. et al. Graphene-antenna sandwich photodetector. *Nano Lett.* **12**, 3808–3813 (2012).
10. Freitag, M. et al. Photocurrent in graphene harnessed by tunable intrinsic plasmons. *Nat. Commun.* **4**, 1951 (2013).
11. Koppens, F. et al. Photodetectors based on graphene, other two-dimensional materials and hybrid systems. *Nat. Nanotechnol.* **9**, 780–793 (2014).
12. Liu, C.-H., Chang, Y.-C., Norris, T. B. & Zhong, Z. Graphene photodetectors with ultra-broadband and high responsivity at room temperature. *Nat. Nanotechnol.* **9**, 273–278 (2014).
13. Goossens, S. et al. Broadband image sensor array based on graphene–CMOS integration. *Nat. Photon.* **11**, 366–371 (2017).
14. Fallahi, A. & Perruisseau-Carrier, J. Design of tunable biperiodic graphene metasurfaces. *Phys. Rev. B* **86**, 195408 (2012).
15. Biswas, S. R. et al. Tunable graphene metasurface reflectarray for cloaking, illusion, and focusing. *Phys. Rev. Appl.* **9**, 034021 (2018).
16. Ju, L. et al. Graphene plasmonics for tunable terahertz metamaterials. *Nat. Nanotechnol.* **6**, 630–634 (2011).
17. Sherrott, M. C. et al. Experimental demonstration of >230° phase modulation in gate-tunable graphene–gold reconfigurable mid-infrared metasurfaces. *Nano Lett.* **17**, 3027–3034 (2017).
18. Bao, Q. et al. Broadband graphene polarizer. *Nat. Photon.* **5**, 411–415 (2011).

19. Tymchenko, M., Nikitin, A. Y. & Martîn-Moreno, L. Faraday rotation due to excitation of magnetoplasmons in graphene microribbons. *ACS Nano* **7**, 9780–9787 (2013).
20. Li, Y. et al. Graphene plasmon enhanced vibrational sensing of surface-adsorbed layers. *Nano Lett.* **14**, 1573–1577 (2014).
21. Rodrigo, D. et al. Mid-infrared plasmonic biosensing with graphene. *Science* **349**, 165–168 (2015).
22. Hu, H. et al. Far-field nanoscale infrared spectroscopy of vibrational fingerprints of molecules with graphene plasmons. *Nat. Commun.* **7**, 12334 (2016).
23. Britnell, L. et al. Strong light–matter interactions in heterostructures of atomically thin films. *Science* **340**, 1311–1314 (2013).
24. Chen, J. et al. Optical nano-imaging of gate-tunable graphene plasmons. *Nature* **487**, 77–81 (2012).
25. Fei, Z. et al. Gate-tuning of graphene plasmons revealed by infrared nano-imaging. *Nature* **487**, 82–85 (2012).
26. Woessner, A. et al. Highly confined low-loss plasmons in graphene–boron nitride heterostructures. *Nat. Mater.* **14**, 421–425 (2015).
27. Hwang, E. & Sarma, S. D. Plasmon modes of spatially separated double-layer graphene. *Phys. Rev. B* **80**, 205405 (2009).
28. Principi, A., Asgari, R. & Polini, M. Acoustic plasmons and composite hole–acoustic plasmon satellite bands in graphene on a metal gate. *Solid State Commun.* **151**, 1627–1630 (2011).
29. Francescato, Y., Giannini, V. & Maier, S. A. Strongly confined gap plasmon modes in graphene sandwiches and graphene-on-silicon. *New J. Phys.* **15**, 063020 (2013).
30. Alonso-González, P. et al. Acoustic terahertz graphene plasmons revealed by photocurrent nanoscopy. *Nat. Nanotechnol.* **12**, 31–35 (2017).
31. Lundeberg, M. B. et al. Tuning quantum nonlocal effects in graphene plasmonics. *Science* **357**, 187–191 (2017).
32. Chen, S. et al. Acoustic graphene plasmon nanoresonators for field-enhanced infrared molecular spectroscopy. *ACS Photon.* **4**, 3089–3097 (2017).
33. Iranzo, D. A. et al. Probing the ultimate plasmon confinement limits with a van der Waals heterostructure. *Science* **360**, 291–295 (2018).
34. Nikitin, A. Y., Low, T. & Martín-Moreno, L. Anomalous reflection phase of graphene plasmons and its influence on resonators. *Phys. Rev. B* **90**, 041407 (2014).
35. Jang, M. S. et al. Tunable large resonant absorption in a midinfrared graphene Salisbury screen. *Phys. Rev. B* **90**, 165409 (2014).
36. Kim, S. et al. Electronically tunable perfect absorption in graphene. *Nano Lett.* **18**, 971–979 (2018).
37. Nagpal, P., Lindquist, N. C., Oh, S.-H. & Norris, D. J. Ultrasmooth patterned metals for plasmonics and metamaterials. *Science* **325**, 594–597 (2009).
38. Lindquist, N. C., Johnson, T. W., Norris, D. J. & Oh, S.-H. Monolithic integration of continuously tunable plasmonic nanostructures. *Nano Lett.* **11**, 3526–3530 (2011).
39. Lee, I.-H. et al. Anisotropic acoustic plasmons in black phosphorus. *ACS Photon.* **5**, 2208–2016 (2017).
40. Yoo, D. et al. High-contrast infrared absorption spectroscopy via mass-produced coaxial zero-mode resonators with sub-10 nm gaps. *Nano Lett.* **18**, 1930–1936 (2018).
41. Adato, R. et al. Ultra-sensitive vibrational spectroscopy of protein monolayers with plasmonic nanoantenna arrays. *Proc. Natl Acad. Sci. USA* **106**, 19227–19232 (2009).
42. Olson, C. & Lynch, D. W. Longitudinal-optical-phonon–plasmon coupling in GaAs. *Phys. Rev.* **177**, 1231 (1969).
43. Perlin, P. et al. Investigation of longitudinal-optical phonon–plasmon coupled modes in highly conducting bulk GaN. *Appl. Phys. Lett.* **67**, 2524–2526 (1995).
44. Passler, N. C. et al. Strong coupling of epsilon-near-zero phonon polaritons in polar dielectric heterostructures. *Nano Lett.* **18**, 4285–4292 (2018).
45. Low, T. et al. Polaritons in layered two-dimensional materials. *Nat. Mater.* **16**, 182–194 (2017).
46. Wang, J., Hernandez, Y., Lotya, M., Coleman, J. N. & Blau, W. J. Broadband nonlinear optical response of graphene dispersions. *Adv. Mater.* **21**, 2430–2435 (2009).
47. Wright, A., Xu, X., Cao, J. & Zhang, C. Strong nonlinear optical response of graphene in the terahertz regime. *Appl. Phys. Lett.* **95**, 072101 (2009).
48. Lim, G.-K. et al. Giant broadband nonlinear optical absorption response in dispersed graphene single sheets. *Nat. Photon.* **5**, 554–560 (2011).
49. Gullans, M., Chang, D., Koppens, F., de Abajo, F. G. & Lukin, M. D. Single-photon nonlinear optics with graphene plasmons. *Phys. Rev. Lett.* **111**, 247401 (2013).
50. Lundeberg, M. B. et al. Thermoelectric detection and imaging of propagating graphene plasmons. *Nat. Mater.* **16**, 204 (2017).
51. Freitag, M., Chiu, H.-Y., Steiner, M., Perebeinos, V. & Avouris, P. Thermal infrared emission from biased graphene. *Nat. Nanotechnol.* **5**, 497–501 (2010).
52. Low, T. & Avouris, P. Graphene plasmonics for terahertz to mid-infrared applications. *ACS Nano* **8**, 1086–1101 (2014).

Acknowledgements

This research was supported primarily by the National Science Foundation (NSF) through an MRSEC grant (to I.-H.L., T.L. and S.-H.O.), ECCS 1809723 (to I.-H.L., S.-H.O. and T.L.) and ECCS 1610333 (to D.Y. and S.-H.O.). T.L. and S.-H.O. also acknowledge support from the Institute for Mathematics and its Applications (IMA) at the University of Minnesota. S.-H.O. further acknowledges support from the Sanford P. Bordeau Endowed Chair at the University of Minnesota. The authors thank S. Kim and M. Jo for sharing silk fibroin samples. Device fabrication was performed at the Minnesota Nanofabrication Center at the University of Minnesota, which receives partial support from the NSF through the National Nanotechnology Coordinated Infrastructure (NNCI). Electron microscopy measurements were performed at the Characterization Facility, which has received capital equipment from NSF MRSEC.

Author contributions

I.-H.L. and S.-H.O. conceived the idea. I.-H.L. performed simulations, device fabrication and characterization. D.Y. performed SEM and AFM characterization. I.-H.L., P.A., T.L. and S.-H.O. performed theoretical analysis. All authors analysed the data and wrote the paper together.

Competing interests

The authors declare no competing interests.

Additional information

Supplementary information is available for this paper at https://doi.org/10.1038/s41565-019-0363-8.

Reprints and permissions information is available at www.nature.com/reprints.

Correspondence and requests for materials should be addressed to S.-H.O.

Methods

Device fabrication. A bare silicon wafer was heated on a hot plate at 180 °C for 5 min before surface activation for 2 min using a standard oxygen plasma cleaning recipe with a reactive ion etcher (Advanced Vacuum, Vision 320). The activated silicon wafer was deposited with a 60-nm-thick gold film as a sacrificial layer using an electron-beam evaporator (CHA Industries, SEC 600). An alumina layer that later defines the gap between metal ribbons and graphene was deposited with an atomic layer deposition (ALD) system (Cambridge Nano Tech). We chose alumina as a gap material due to its low optical absorption at the operating frequencies and its compatibility with ALD systems, and the fact that it can grow ultrasmooth films with ångström-scale thickness control. The large refractive index (~3.3) and low mid-infrared absorption of the amorphous silicon used for the optical spacer reduce the thickness required for the quarter-wavelength condition and minimize optical loss in the substrate. The index-matching layer increases the transmission of light through the metal ribbon array in the presence of a high-index substrate so that more light can be recoupled to plasmons after reflection from the back reflector. To fabricate metal ribbons, a 30-nm-thick gold film was deposited on the alumina layer via sputtering (AJA, ATC 2200). On top of the gold layer, an electron-beam resist, polymethyl methacrylate (MicroChem, 950 PMMA C2), was spin-coated at a rate of 4,000 r.p.m. for 30 s. After baking at 180 °C for 2 min, the PMMA layer was exposed to electron beams at 100 keV energy with an exposure dose of 1,400 μC cm^{-2} using an electron-beam lithography system (Vistec, EBPG5000+). The sample was then developed with a solution of MIBK:IPA (1:3) for 60 s to generate a PMMA ribbon array. Using the PMMA ribbon array as a mask, the sputtered gold film was etched using an ion milling process (Intlvac, Nanoquest), using Ar^+ ions at a beam current of 70 mA and an accelerating voltage of 24 V. The PMMA etch mask was removed by the oxygen plasma cleaning process mentioned above.

The resultant metal ribbon arrays were sequentially covered by 20-nm-thick alumina, 1-nm-thick SiO_2 and amorphous silicon (typically a few hundreds of nanometres) and a 1-nm-thick titanium and 90-nm-thick gold layer using ALD, plasma-enhanced chemical vapour deposition (Plasma-Therm, PECVD) and sputterer, respectively. The 1-nm-thick SiO_2 promotes adhesion between the alumina and amorphous silicon layer. Next, we used a template stripping method using a photocurable epoxy (Norland, NOA 61) as an adhesive to transfer the entire device to a glass substrate. This peeling process caused the bottom interface between the silicon wafer and the sacrificial layer to be exposed to the top of the transferred device. The sacrificial layer was then removed by a wet etching process using a gold etchant (Sigma Aldrich) to reveal the alumina layer on metal ribbons. Finally, a graphene sheet on a copper foil (Graphene Supermarket) was transferred onto the alumina layer using the wet-transfer method[53]. For SEIRA experiments, an aqueous solution of silk-fibroin molecules was prepared according to previous work[40] and spin-coated on the template-stripped substrate before transferring graphene. For the plasmon–phonon coupling experiment, we deposited a 0.2- and 0.3-nm-thick SiO_2 film using sputtering (AJA, ATC 2200) at a rate of 1.3 nm min^{-1}. The fabricated devices were chemically doped[54] by exposure to vapours from a nitric acid solution for 5 min (ref. [55]). We used the chemical doping method to ensure that the doping levels of different devices were identical, which allowed us to explore the dependence on various geometrical parameters such as gap size, ribbon width and thickness of the analytes. Note that electrical doping is also possible, by applying a voltage across the metal ribbons and a graphene layer (Supplementary Fig. 19).

Device characterization. The spectra of our devices were measured using Fourier-transform infrared spectroscopy (Thermo Scientific, Nicolet Magna IR 750) in reflection mode. We used a microscope with an infrared light source, a liquid-N_2-cooled MCT-A (mercury cadmium telluride) detector, and an aperture size of 100 μm by 100 μm. The signals were averaged over 200 scans with a resolution of 2 cm^{-1} and were normalized to the background signal taken from a thick gold film. We used SEM (Hitach, SU-8230) to characterize the critical dimensions and inspect how well the functional layers were defined. The surface roughness of the template-stripped substrates was characterized using tapping-mode AFM (Bruker, DI5000). The thickness of the silk and SiO_2 films was characterized using an ellipsometer (Gaertner Scientific Corp.; 7109-C370B).

Numerical simulation. We used rigorous coupled wave analysis implemented in MATLAB (MathWorks) for calculation of the electric field distribution and absorption in Figs. 1 and 2, the inset in Fig. 4c and Fig. 5. The optical conductivities of graphene were calculated using random-phase approximation at 300 K (ref. [56]; Supplementary Fig. 20). The doping level and damping rate for graphene were −0.63 eV and 0.03 fs^{-1} for all simulations, except in Fig. 5, where we used higher damping rate of 0.05 fs^{-1} for the 3-nm-thick silk film, and 0.07 fs^{-1} for the 0.8-nm-thick silk case. In our experimental regime, the non-local effects were found to be negligible (Supplementary Fig. 21). The refractive indices for gold[57] and alumina[58] were taken from the literature. The refractive index of an amorphous silicon layer was assumed to be the dispersionless value of 3.3. For Fig. 5, we generated the refractive indices of silk using the parameters extracted by fitting the experimentally measured data[59].

Data availability

The data that support the plots within this paper and other findings of this study are available from the corresponding author upon reasonable request.

References

53. Liang, X. et al. Toward clean and crackless transfer of graphene. *ACS Nano* **5**, 9144–9153 (2011).
54. Gunes, F. et al. Layer-by-layer doping of few-layer graphene film. *ACS Nano* **4**, 4595–4600 (2010).
55. D'Arsié, L. et al. Stable, efficient p-type doping of graphene by nitric acid. *RSC Adv.* **6**, 113185–113192 (2016).
56. Nikitin, A. Y., Guinea, F., Garcia-Vidal, F. & Martin-Moreno, L. Fields radiated by a nanoemitter in a graphene sheet. *Phys. Rev. B* **84**, 195446 (2011).
57. Ordal, M. A., Bell, R. J., Alexander, R. W., Long, L. L. & Querry, M. R. Optical properties of Au, Ni, and Pb at submillimeter wavelengths. *Appl. Opt.* **26**, 744–752 (1987).
58. Kischkat, J. et al. Mid-infrared optical properties of thin films of aluminum oxide, titanium dioxide, silicon dioxide, aluminum nitride, and silicon nitride. *Appl. Opt.* **51**, 6789–6798 (2012).
59. Liberman, V. et al. Rational design and optimization of plasmonic nanoarrays for surface enhanced infrared spectroscopy. *Opt. Express* **20**, 11953–11967 (2012).